Acta Materialia 302 (2026) 121687

Contents lists available at ScienceDirect

Acta Materialia

journal homepage: www.elsevier.com/locate/actamat

Zero thermal expansion and magnetocaloric effect in B doped $Fe_2(Hf,Ta)$ Laves phase compounds

Qi Shen [a], Zeyu Zhang [a], Weixiang Hao [a], Niels van Dijk [b], Ekkes Brück [b], Lingwei Li [a,*]

[a] Key Laboratory of Novel Materials for Sensor of Zhejiang Province, Hangzhou Dianzi University, Hangzhou, 310012, PR China
[b] Fundamental Aspects of Materials and Energy, Faculty of Applied Sciences, Delft University of Technology, Mekelweg 15, 2629 JB Delft, the Netherlands

ARTICLE INFO

Keywords:
Magnetoelastic transition
Zero thermal expansion
Magnetocaloric effect

ABSTRACT

Materials with zero thermal expansion (ZTE) or negative thermal expansion (NTE) are critical for precision applications. Magnetocaloric materials exhibiting a strong spin-lattice coupling often undergo lattice changes near a magnetic transition, offering a route to ZTE behavior via magnetoelastic effects. This study examines the effect of Boron doping on the magnetoelastic transition, thermal expansion and magnetocaloric properties in $Fe_{1.98}Hf_{0.85}Ta_{0.15}B_x$ (x = 0.00, 0.01, 0.02, 0.03, 0.04) Laves phase alloys. Boron doping enhances hardness and increases the field sensitivity of the transition temperature. The second-order transition in the undoped alloy evolves into a first-order ferromagnetic-antiferromagnetic transition upon doping. First-principles calculations show that B occupies the 2*a* sites, modifying the Fe-Hf 3*d*-5*d* hybridization and strengthening the spin-lattice coupling. In the $Fe_{1.98}$ $Hf_{0.85}Ta_{0.15}B_{0.01}$ alloy a near-zero thermal expansion with a coefficient of −0.17 ppm/K is observed in a temperature range of 133–213 K below the magnetoelastic transition at T_t = 266 K, which is ascribed to the enhanced magnetoelastic transition by light-element doping with B. Our findings highlight a promising strategy to optimize the ZTE behavior through targeted light-element doping in magnetocaloric Laves phase systems.

1. Introduction

Negative thermal expansion (NTE) materials have attracted considerable attention due to their unusual property of contracting upon heating, which contrasts sharply with the typical positive thermal expansion (PTE) observed in most materials. This counterintuitive behavior makes NTE materials highly valuable for thermal expansion compensation in various advanced technologies. Zero thermal expansion (ZTE) materials, often engineered by combining NTE and PTE phases, are of particular importance in applications requiring exceptional dimensional stability across a broad temperature range, including dental prosthetics, high-precision optical components, and printed electronics. Since the pioneering discovery of magnetic Invar alloys in 1897, a variety of novel magnetic ZTE materials have been identified [1].

The magnetocaloric effect (MCE) describes the thermal response of a material to an applied or removed magnetic field, typically quantified by the magnetic entropy change and the adiabatic temperature change [2–6]. Many magnetocaloric materials also exhibit excellent ZTE behavior due to significant lattice expansion or contraction associated with a magnetic transition [7–9]. Compounds like La(Fe,Si)-based compounds [10–13], Fe-based Laves phases [7,14–21], Mn-based antiperovskites [22,23], and Rare-Earth-based alloys [8,24] display a tunable magnetoelastic transition, allowing control of the thermal expansion. These materials exemplify the strong interplay between magnetic ordering and lattice strain that underpins both MCE and ZTE functionalities.

Among the various magnetic zero/negative thermal expansion (ZTE/NTE) materials, non-rare-earth $Fe_2(Hf,Ta)$ alloys have emerged as particularly promising due to their advantageous combination of high electrical and thermal conductivities, as well as robust mechanical properties [25]. The NTE behavior in these alloys originates from a magnetoelastic transition, specifically a transformation from a large-volume ferromagnetic (FM) state to a smaller-volume antiferromagnetic (AFM) state with increasing temperature [14,25]. An optimized composition, $Fe_2Hf_{0.87}Ta_{0.13}$, exhibits a pronounced linear NTE coefficient of –16.3 ppm/K over a wide temperature interval of 105 K (222–327 K) [25]. Additionally, a broad ZTE region characterized by a low thermal expansion coefficient of 0.16 ppm/K has been observed in $Fe_{1.88}Al_{0.12}Hf_{0.9}Ta_{0.1}$ alloy within a temperature range of 272–378 K

* Corresponding author at: Key Laboratory of Novel Materials for Sensor of Zhejiang Province, Hangzhou Dianzi University, Hangzhou, 310012, PR China.
E-mail address: lingwei@hdu.edu.cn (L. Li).

https://doi.org/10.1016/j.actamat.2025.121687
Received 28 May 2025; Received in revised form 12 September 2025; Accepted 27 October 2025
Available online 28 October 2025

[26]. Despite these encouraging results, a systematic understanding of the effects of light-element doping on the thermal expansion behavior in this system remains scarce.

In the present study, we explore the influence of incorporating the small-sized B element into the $Fe_2Hf_{0.85}Ta_{0.15}$ alloy matrix to modulate its ZTE properties. Our findings demonstrate that B doping yields a near-zero thermal expansion coefficient (CTE) of –0.17 ppm/K in the temperature range 133–213, below the magnetoelastic transition at T_C = 266 K, underscoring its potential as an effective strategy for fine-tuning ZTE behavior in Fe_2(Hf,Ta)-based systems.

2. Experimental methods

Polycrystalline $Fe_{1.98}Hf_{0.85}Ta_{0.15}B_x$ (x = 0.00, 0.01, 0.02, 0.03, 0.04) samples were prepared from high-purity elements (Fe 99.98 %, Mn 99.9 %, Hf 99.7 %, Ta 99.7 %,) by arc melting. Slightly off-stoichiometric Fe compositions favor a sharper magnetic transition [27]. The alloys were prepared by arc-melting approximately 5 g of starting materials under an argon atmosphere. To ensure homogeneity, each button-shaped sample was melted four to five times. The samples were flipped after each melt. For ease of reference, the x = 0.00, 0.01, 0.02, 0.03, 0.04 samples are denoted as B0.00, B0.01, B0.02, B0.03 and B0.04 alloys, respectively. Previous studies on $Fe_2Hf_{0.83}Ta_{0.17}$ [28] and the comparison in *M-T* curves of annealed and unannealed B0.00 alloys are shown in Fig. S1 and indicate that the heat treatment had minimal effect on the magnetic properties. Therefore, no additional annealing was performed on these samples.

X-ray diffraction (XRD) data were collected with a Smartlab diffractometer using Cu-K_α radiation and an Anton Paar TTK 450 temperature chamber. Rietveld refinement was performed using the FullProf software suite [29]. The magnetic properties of the samples were measured over a temperature range of 4–370 K using a superconducting quantum interference device (SQUID) magnetometer (MPMS-Q3) equipped with a reciprocating sample option. The ferromagnetic transition temperature was determined from the minimum in the derivative of the magnetization-temperature (*M-T*) curves. Magnetic entropy changes were calculated from *M-T* curves measured at various magnetic field strengths, using the Maxwell relation. Differential scanning calorimetry (DSC) measurements were performed using a TA-Discovery DSC 25 calorimeter. The microstructure was examined with an Electron Probe X-ray Micro-Analyzer (EPMA, JXA-iHP200F JEOL), equipped with Wavelength Dispersive X-ray Spectroscopy (WDS). The Vickers hardness measurements of the B0.00 and B0.01 samples were performed on the MVS-50Z Vickers hardness tester (19.61 N, 15 s).

First-principles calculations based on DFT calculations were conducted to investigate the electronic and magnetic structures of Fe-Hf-Ta-B alloys. The DFT calculations were performed using the Vienna Ab Initio Simulation Package (VASP) [30,31] with a plane-wave basis sets. An energy cutoff of 520 eV was applied, and pseudopotentials were defined using the projected augmented wave (PAW) method with valence configurations $3d^6\ 4s^2$ for Fe, $5d^2\ 6s^2$ for Hf, $5d^3\ 6s^2$ for Ta and $2p^1 4s^2$ for B [32,33]. Exchange-correlation interactions were modeled using the Perdew-Burke-Ernzerhof (PBE) functional within the generalized gradient approximation (GGA), and a Monkhorst-Pack $\boldsymbol{k}$-point grid of 9 × 9 × 1 based on a 60-atom supercell was employed for both structural optimization and electronic properties calculations [34]. Convergence criteria for the Hellmann-Feynman forces were set at <0.01 eV/Å, with an electronic loop convergence threshold of 10^{-5} eV. The formation energy E_f was calculated as follows: $E_f = E_{\text{compound}} - \sum_i x_i E_i$, where E_{compound} represents the optimized total energy of the compound, and x_i and E_i are the stoichiometric coefficients and ground-state energies of Fe, Hf, Ta, and B atoms in their reference states, respectively. A lower E_f indicates a higher stability of the alloy, which can be used to obtain the preferred atomic site occupations.

To investigate the nature of chemical bonding, the Electron Localization Function (ELF) [35] was analyzed. The ELF quantifies the likelihood of finding a second electron with the same spin near a reference electron, based on the Pauli exclusion principle. High ELF values correspond to regions of strong electron localization, indicating a covalent character in the bonding.

3. Results and discussion

Fig. 1(a) shows the XRD patterns of $Fe_{1.98}Hf_{0.85}Ta_{0.15}B_x$ (x = 0.00, 0.01, 0.02, 0.03, 0.04) alloys at room temperature, confirming that all samples crystallize in a hexagonal $MgZn_2$-type Laves structure (space group: $P6_3/mmc$). The refined XRD pattern of the B0.01 sample is shown in Fig. 1(b). As illustrated in Fig. 1(c) and 1(d), increasing the B content results in a clear contraction of the lattice volume, attributed to the substitutional incorporation of B atoms. The *a* axis decreases, while the *c* axis remains nearly unchanged. Fig. 1(d) also presents a schematic of the primary unit cell, where Fe atoms occupy the 2*a* and 6*h* sites, and the Hf/Ta atoms are located at the 4*f* site. The local atomic environments of Fe at the 2*a* and 6*h* sites are shown in Fig. S2, where the interatomic distances of 2.448 Å and 2.471 Å are observed between the Fe_{6h}-Fe_{6h} atoms and Fe_{2a}-Fe_{6h} atoms, respectively.

To further evaluate the homogeneity of the alloys, EPMA was performed on all samples, as shown in Fig. 2. The atomic composition of the matrix provided in Fig. 2(f), reveals a good agreement with the nominal composition. A systematic increase in B content confirms the incorporation of B into the matrix. The Hf content is about 1 % lower than the nominal composition, which can be attributed to the presence of a minor white secondary phase identified by WDS analysis as Hf-rich. The detailed compositions and phase fractions of the secondary phase are summarized in Table S1. The overall secondary phase content in all alloys remains below the detection limit of XRD. The B0.00, B0.01, and B0.02 alloys contain <1 % of the Hf-rich secondary phase, with B0.01 exhibiting a smaller fraction than B0.00 and B0.02. In contrast, B0.03 and B0.04 contain higher amounts of the secondary phase of 1.4 % and 2.4 %, respectively (mainly located at the grain boundaries). Notably, the B-rich phase in the white region (corresponding WDS points are shown in Fig. S3) was identified in B0.03 and B0.04, as listed in Table S1. This suggests that x = 0.02 corresponds to the solubility limit of B in the $Fe_{1.98}Hf_{0.85}Ta_{0.15}B_x$ alloys.

Fig. 3(a, b) display the *M-T* curves of $Fe_{1.98}Hf_{0.85}Ta_{0.15}B_x$ (x = 0.00–0.04) alloys measured under magnetic fields of 0.01 T and 1 T The transition temperature (T_t) upon cooling curves, determined from both *M-T* curves and DSC measurements (as shown in Fig. S4), decreases for x < 0.02 and then increases with further B addition. In a 1 T magnetic field, T_t values are 7–10 K higher than those from DSC, due to enhanced ferromagnetic ordering in the applied field. This variation in T_t aligns with the changes in lattice volume V in Fig. 1(c). The saturation magnetization of 44.18 Am^2/kg for the B0.02 alloy is significantly reduced from 58.00 Am^2/kg for the B0.00 alloy and 57.21 Am^2/kg for the B0.01 alloy. The M_s values for B0.03 and B0.04 are 49.37 Am^2/kg and 51.02 Am^2/kg, respectively. The increase in M_s for B0.03 and B0.04 compared to B0.02 is attributed to the presence of a ferromagnetic secondary phase of B-rich phase at the grain boundaries by EMPA analysis, corresponding to the residual magnetic signal above T_t in Fig. 3 (b).

Fig. 4(a-c) shows the *M-T* curves of the B0.00, B0.01, and B0.02 alloys measured under magnetic fields ranging from 0.2 to 5 T With increasing B content, the transition curves shift toward lower temperatures, indicating a suppression of the ferromagnetic phase due to B doping. The corresponding Arrott plots, derived from the *M-T* data, are presented in Fig. 4(d-f). According to Banerjee's criterion, a positive slope indicates a second-order magnetic transition (SOMT), while a negative slope indicates a first-order magnetic transition (FOMT). The B0.00 alloy displays Arrott plots with positive slopes, suggesting a SOMT behavior. In contrast, the B0.01 and B0.02 alloys exhibit negative slopes, indicative of FOMT characteristics.

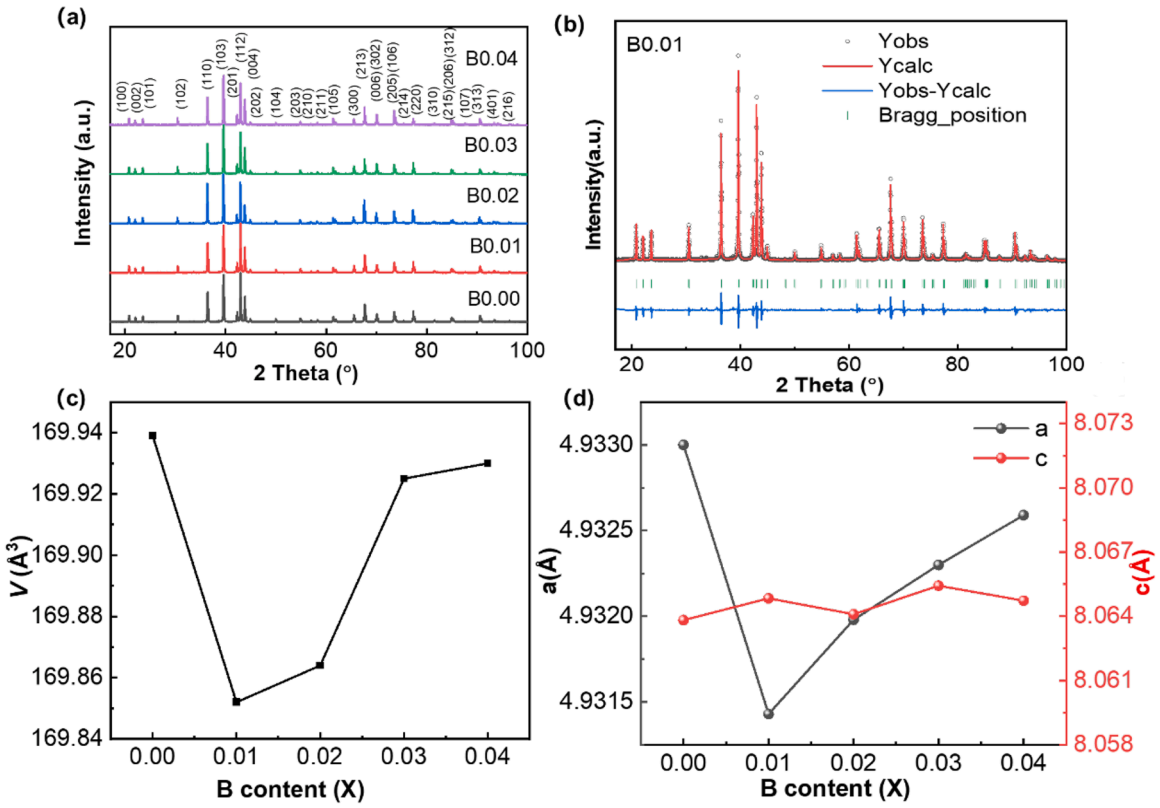

Fig. 1. (a) XRD patterns of $Fe_{1.98}Hf_{0.85}Ta_{0.15}B_x$ (x = 0.00, 0.01, 0.02, 0.03, 0.04) alloys, with indexed peaks of the $MgZn_2$-type structure. (b) Refined XRD pattern of the B0.01 alloy. (c) Lattice volume (V) and (d) lattice parameters (a and c) as a function of B content.

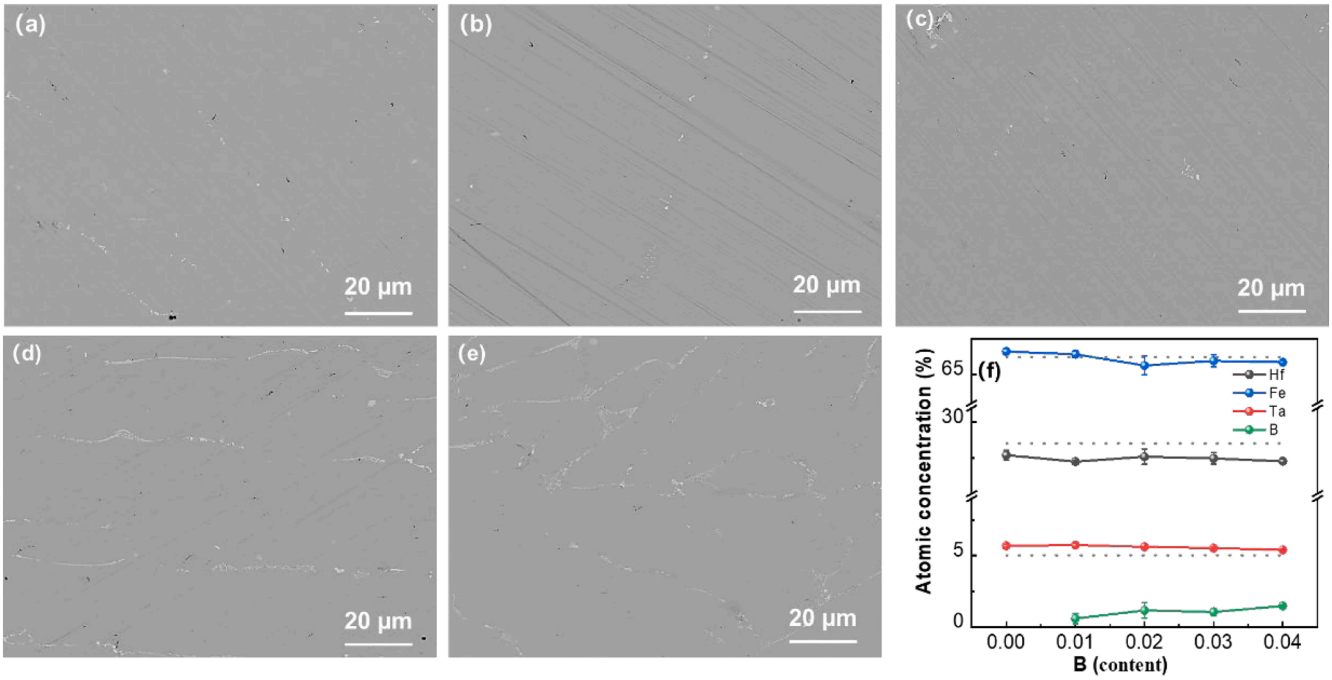

Fig. 2. The microstructure of (a) B0.00, (b) B0.01, (c) B0.02, (d) B0.03, (e) B0.04 alloys (f) The atomic concentration of matrix by WDS. The dashed line is the nominal composition.

The order of the magnetic transition can also be evaluated using the field exponent n, as proposed by Law and co-authors [36], where n is determined from the relation: $n\ (T,\ H) = \frac{d\ln|\Delta S_M|}{d\ln H}$. The temperature dependence of n is shown in Fig. 4(a). A maximum field exponent of $n >$ 2 indicates a FOMT, while $n < 2$ corresponds to a SOMT. For the B0.00 alloy, n remains below 2 across the measured range, confirming its SOMT character. In contrast, B0.01 and B0.02 both show a clear maximum above $n = 2$, consistent with the FOMT behavior and in

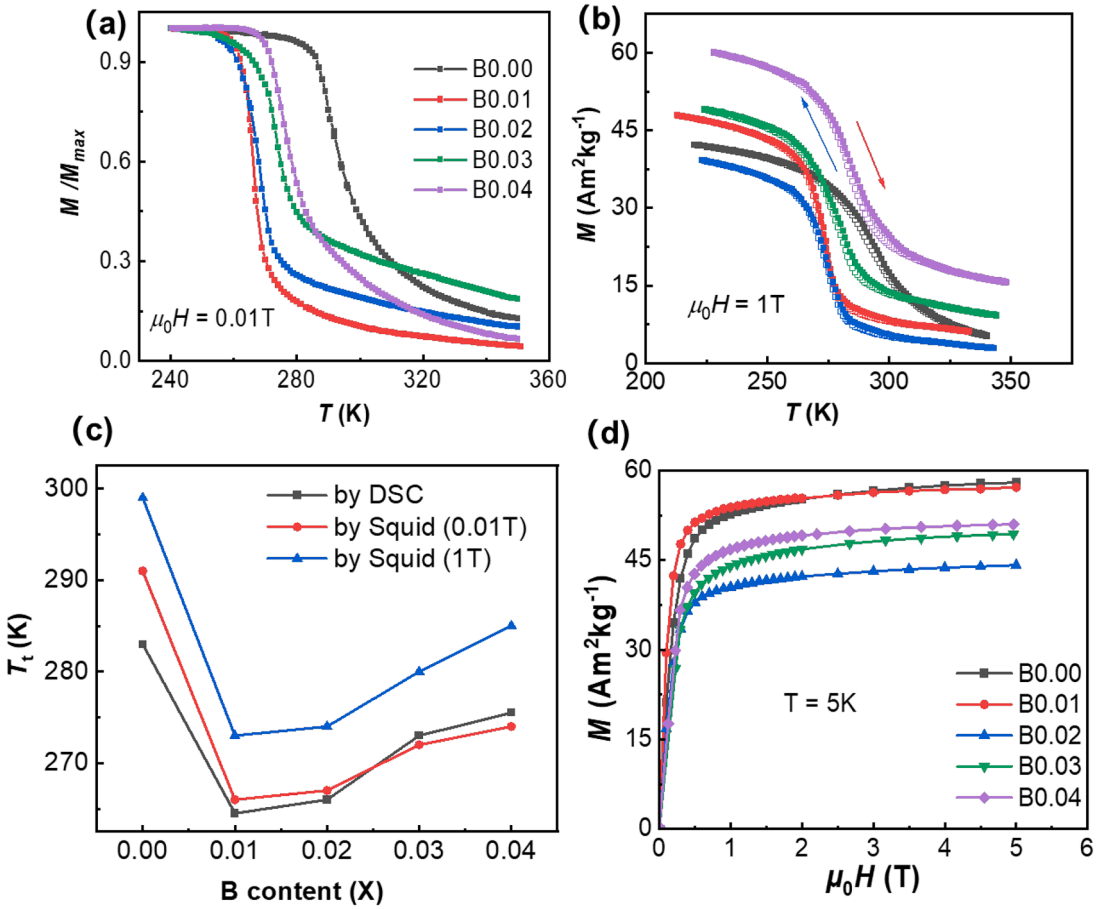

Fig. 3. *M-T* curves for the $Fe_{1.98}Hf_{0.85}Ta_{0.15}B_x$ (x = 0.00–0.04) alloys in magnetic fields of (a) 0.1 T (*M-T* curves are normalized for comparison of transition temperatures) and (b) 1 T The open-symbol curve with the blue arrow and the solid curve with the red arrow represent the cooling and heating processes, respectively. (c) Variation in phase transition temperature calculated from DSC and *M-T* curves in applied magnetic fields of 0.01 T and 1 T (d) *M-H* curves for the $Fe_{1.98}Hf_{0.85}Ta_{0.15}B_x$ (x = 0.00–0.04) alloys at 5 K.

agreement with the Arrott plot analysis. Fig. 5(b) presents the calculated $-\Delta S_M$ curves for the alloys. All alloys exhibit pronounced peaks near their respective phase transition temperatures. The maximum $|\Delta S_M|$ values increase with increasing magnetic field change ($\Delta\mu_0 H$). Specifically, for the B0.00 alloy, maximum $|\Delta S_M|$ values of 1.79 J/kgK and 3.91 J/kgK were obtained for $\Delta\mu_0 H$ = 2 T and 5 T, respectively. For the B0.01 alloy, the maximum $|\Delta S_M|$ values reach 3.13 J/kgK and 4.29 J/kgK, while for the B0.02 alloy, they are 2.73 J/kgK and 4.13 J/kgK. The $|\Delta S_M|$ value is larger than for other non-rare-earth alloys, like $Mn_{30}Fe_{20-x}Cu_xAl_{50}$ ($|\Delta S_M|$ = 1.4 J/kgK for a field change of 2 T) [37], and is comparable to other Fe_2(Hf,Ta)-based alloys with 1–5 J/kgK for a field change of 2 T [7,38,39], Mn_2Sb-based alloys with 2–7 J/kgKfor a field change of 5 T [40,41] and Gd metals with 6.1 J/kgK for a field change of 2 T [42].

The field dependence of the transition temperature, quantified by $m = dT_t/d\mu_0 H$, is shown in Fig. 5(c). The B0.01 alloy exhibits the highest m value of 8.4 K/T, whereas the B0.00 alloy shows a much lower m value of 3.2 K/T, consistent with its SOMT nature. A positive correlation between the n value and m is observed, indicating that stronger field sensitivity aligns with a more pronounced FOMT character. In addition to the magnetic properties, the mechanical strength was evaluated via Vickers hardness measurements, as shown in Fig. 5(d). The B0.01 and B0.00 alloys exhibit average hardness values of 962 HV and 915 HV, respectively. Both hardness values are significantly higher than those reported for $Fe_{0.65}Ni_{0.35}$ [1] and $ErCo_{2.8}Fe_{0.2}$ [8], indicating an enhanced resistance to plastic deformation by B doping in Fe_2(Hf,Ta) alloys.

To elucidate the influence of B doping on both the magnetic and structural stability in the Fe_2(Hf,Ta) system, DFT calculations were performed on $Fe_{2-x}Hf_{0.85}Ta_{0.15}B_x$ compositions with x = 0.00 and 0.05. The site-dependent formation energies, optimized lattice parameters, and magnetic moments were evaluated. As shown in Fig. 6(a), B atoms exhibit a strong site preference for the 2*a* position, which corresponds to the lowest formation energy. The calculated formation energy difference between the 6*h* and 2*a* sites in $Fe_{1.95}Hf_{0.85}Ta_{0.15}B_{0.05}$ is 16.5 meV/f.u. (5.5 meV for the 60-atom supercell). To better probe the effect of B on site preference and magnetism, we also considered a larger, "exaggerated" substitution of $Fe_{1.5}Hf_{0.85}Ta_{0.15}B_{0.50}$ at both the 6*h* and 2*a* sites. The result shows an even larger formation energy difference of 54 meV/f.u. Both values consistently indicate a clear energetic preference of B for the 2*a* site. Replacing Fe by B in $Fe_{1.95}Hf_{0.85}Ta_{0.15}B_{0.05}$ leads to a calculated unit-cell volume of 157.90 Å^3, smaller than that of the undoped $Fe_2Hf_{0.85}Ta_{0.15}$ (159.11 Å^3) alloy, consistent with experimental XRD results. The total density of states (TDOS) in the ferromagnetic state, shown in Fig. 6(b), confirms its metallic behavior with a significant TDOS at the Fermi level and net magnetic moments of 3.10 μ_B/f.u. and 3.08 μ_B/f.u. for the $Fe_{1.95}Hf_{0.85}Ta_{0.15}B_{0.05}$ and $Fe_2Hf_{0.85}Ta_{0.15}$ systems, respectively. The slight reduction in the calculated magnetic moment with B doping aligns with the decreasing trend in M_s observed experimentally (58.00 Am^2/kg for B0.00, 57.21 Am^2/kg for B0.01, and 44.18 Am^2/kg for B0.02). The PDOS shown in Fig. 6(c) and in Fig. S5 for the B-free alloy and weakly B-doped alloy exhibit similar profiles. In contrast, the PDOS in Fig. 6(d) for excess B-doped alloy shows a substantial modification of the Fe 6*h*-projected density of states, accompanied by a significant reduction in the net moment to 1.95 μ_B/f.u.

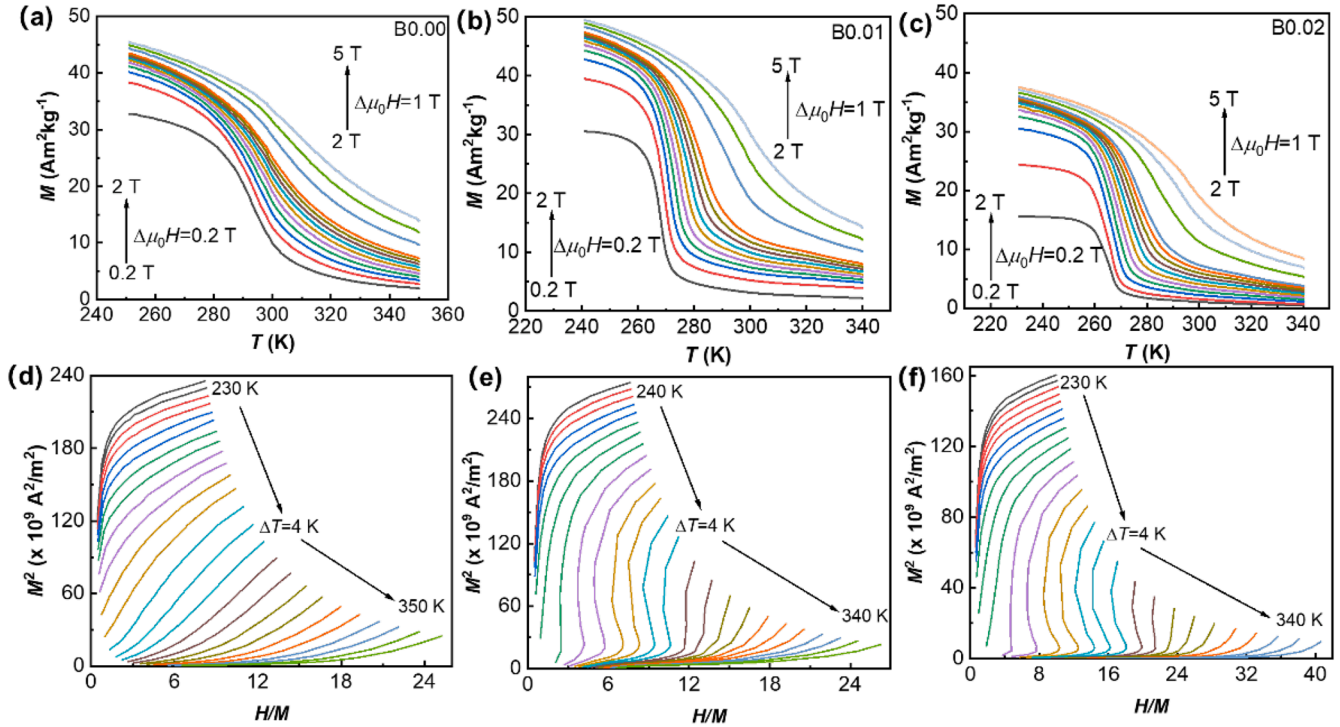

Fig. 4. *M-T* curves upon heating in different applied magnetic fields for (a) B0.00, (b) B0.01 and (c) B0.02 alloys. Arrott plots calculated from heating curves for (d) B0.00, (e) B0.01 and (f) B0.02 alloys.

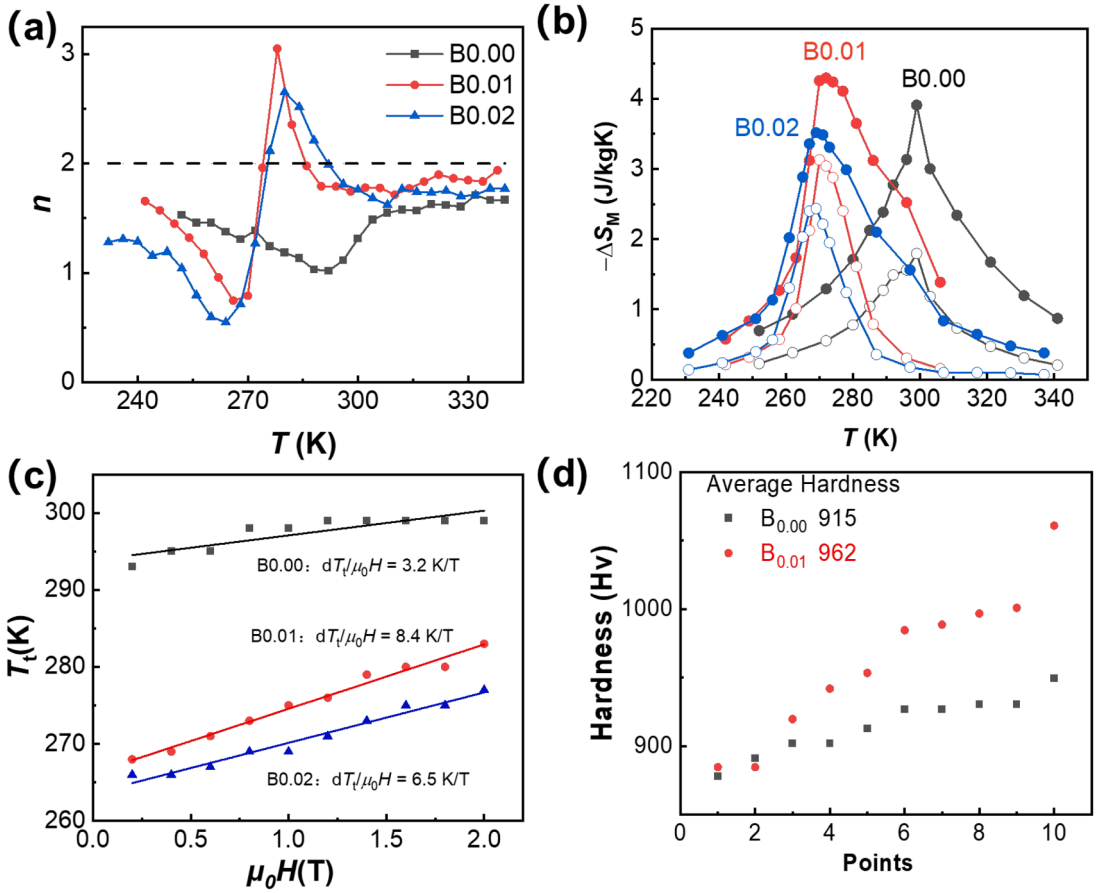

Fig. 5. (a) Field exponent *n* as a function of temperature for the B0.00, B0.01 and B0.02 alloys in a magnetic field of 2 T (b) -ΔS_M(T) curves of the B0.00, B0.01 and B0.02 alloys at a magnetic field of 2 T and 5 T (c) T_t as a function of magnetic field. (d) Vickers hardness for the B0.00 and B0.01 alloys in ordered hardness magnitude.

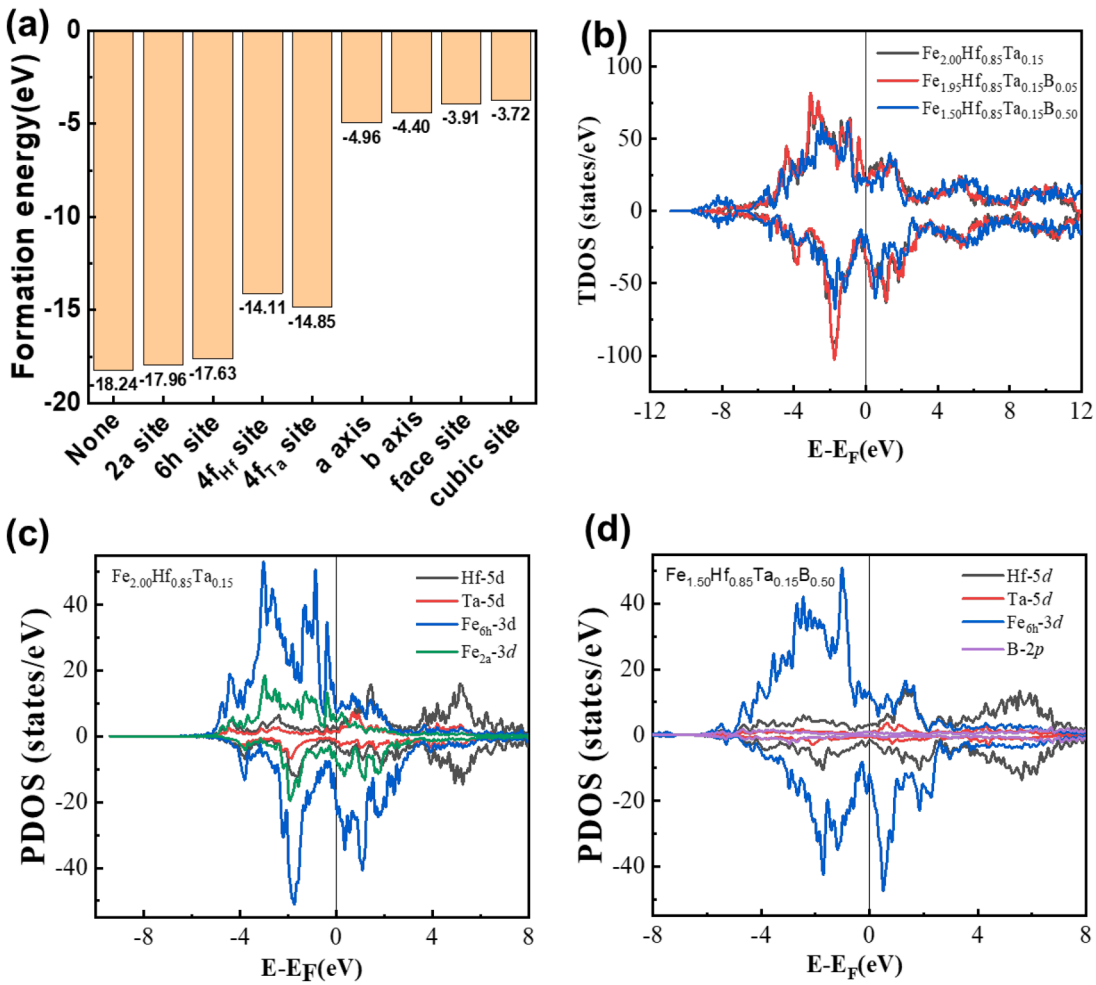

Fig. 6. (a) Formation energies E_f of 60-atoms supercell for B substitution at the 2*a*, 6*h* , 4*f* sites and interstitial sites in $Fe_{2.00}Hf_{0.85}Ta_{0.15}$, showing that the 2*a* site is energetically preferred. (b) Total density of states (TDOS) in the ferromagnetic state for the undoped $Fe_{2.00}Hf_{0.85}Ta_{0.15}$ and B-doped $Fe_{1.95}Hf_{0.85}Ta_{0.15}B_{0.05}$ and $Fe_{1.50}Hf_{0.85}Ta_{0.15}B_{0.50}$ alloys. (c) Orbital-projected DOS (PDOS) for the undoped alloy, highlighting Fe-3*d* and Hf/Ta-4*d* contributions. (d) PDOS for the B-doped alloys, showing B-2*p* states and the altered Fe-3*d* and Hf/Ta-4*d* hybridization. In (b–d), the vertical line marks the Fermi level ($E_F = 0$ eV).

Therefore, excess B doping not only contracts the lattice and distorts the electronic structure but also leads to a pronounced reduction in saturation magnetization, ultimately weakening the magnetocaloric performance.

The electron localization function (ELF), a tool grounded in valence shell electron pair repulsion theory, has previously been used to distinguish covalent versus metallic bonding in intermetallics, such as F or S doped $(Mn,Fe)_2(P,Si)$ [43] and Cu doped MnCoGe [44]. To examine how B doping influences the magnetic transition behavior in $Fe_2(Hf,Ta)$, the ELF of a hexagonal $Fe_{1.95}Hf_{0.85}Ta_{0.15}B_{0.05}$ supercell was analyzed, as shown in Fig. 7. The 2D ELF contour plots in Fig. 7(a-d), sliced along the (001) and (110) planes, reveal increased electron localization around B atoms in the doped system, with peak ELF values around 0.5. ELF line profiles in Fig. 7(e-f), extracted between Fe atoms at 2*a* and 6*h* sites and their nearest neighbors, show an enhanced electron localization at both sites upon B doping. Interestingly, the localization between Fe(2*a*) and Hf weakens, as evidenced by a 5.6 % decrease in the maximum ELF peak value, whereas it is strengthened between Fe(6*h*) and Hf, showing a 5.0 % increase. This indicates a site-selective modulation of *d*–*d* hybridization. Such a competitive bonding environment, introduced by B atoms, may contribute to the FOMT observed in the B-doped $Fe_2(Hf,Ta)$ system [45].

In $Fe_2(Hf,Ta)$, which undergoes a FM-AFM transition, the FM state has a larger unit-cell volume than the frustrated AFM state. This volume mismatch across the transition leads to a net negative contribution to the thermal expansion, providing a natural basis for ZTE or NTE behavior [46]. Therefore, temperature-dependent XRD measurements were performed on the B0.00, B0.01, and B0.02 alloys at 20 K intervals across the transition range. Structural refinement confirms that all samples retain the hexagonal *C*14 Laves phase throughout the measured temperature range. As shown in Fig. 8(e-f), the appearance of peak splitting at 253 K in the B0.01 and B0.02 alloys provides direct evidence for a FOMT, while the smooth evolution of the diffraction patterns in the B0.00 alloy supports the presence of a SOMT. Fig. 9 presents the lattice parameters and unit-cell volumes of the alloys. In the B0.00 alloy, a continuous decrease in the lattice parameter *a* and an increase in *c* is observed, whereas the B0.01 and B0.02 alloys exhibit discontinuous trends. For the B0.01 and B0.02 alloys, the change in the *V-T* curve at $T_N = 333$ K responses to the AFM-PM transition [14,28]. The B0.00 alloy exhibits a continuous volume contraction between 193 and 313 K, corresponding to a negative CTE of $\alpha_v = -29.6$ ppm/K. This NTE originates directly from the volume collapse associated with the FM-AFM transition. In contrast, the B0.01 alloy undergoes a FOMT, as confirmed by both the *n*-value and Arrott-plot analysis, and displays a larger magnetic entropy change ($-\Delta S_M = 3.13$ J/kg·K at 2 T) compared with the B0.00 alloy (1.79 J/kg·K at 2 T) with a SOMT. This strong magnetoelastic coupling stabilizes a near-zero CTE ($\alpha_V = -0.17$ ppm/K) in the range 133–213 K below the transition temperature. The estimated linear CTE α_l based on the relation $\alpha_l = \alpha_V/3$ is 1.37 ppm/K, 0.06 ppm/K and 1.17 ppm/K for B0.00, B0.01 and B0.02, respectively [47].

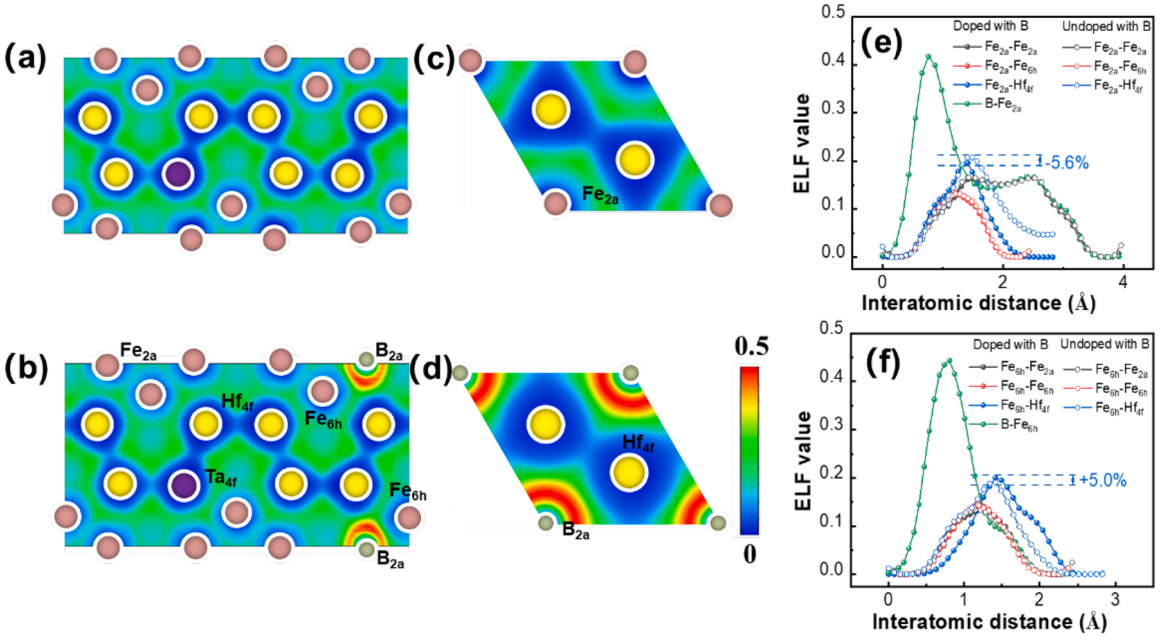

Fig. 7. 2D ELF contour maps in the ferromagnetic state for $Fe_2(Hf,Ta)$ alloys, comparing undoped and B-doped supercells: (a) undoped, (b) B-doped along the (110) plane; (c) undoped, (d) B-doped along the (001) plane. Line profiles of the ELF values between Fe and its nearest neighbors for (e) Fe at the 2*a* site and (f) Fe at the 6*h* site.

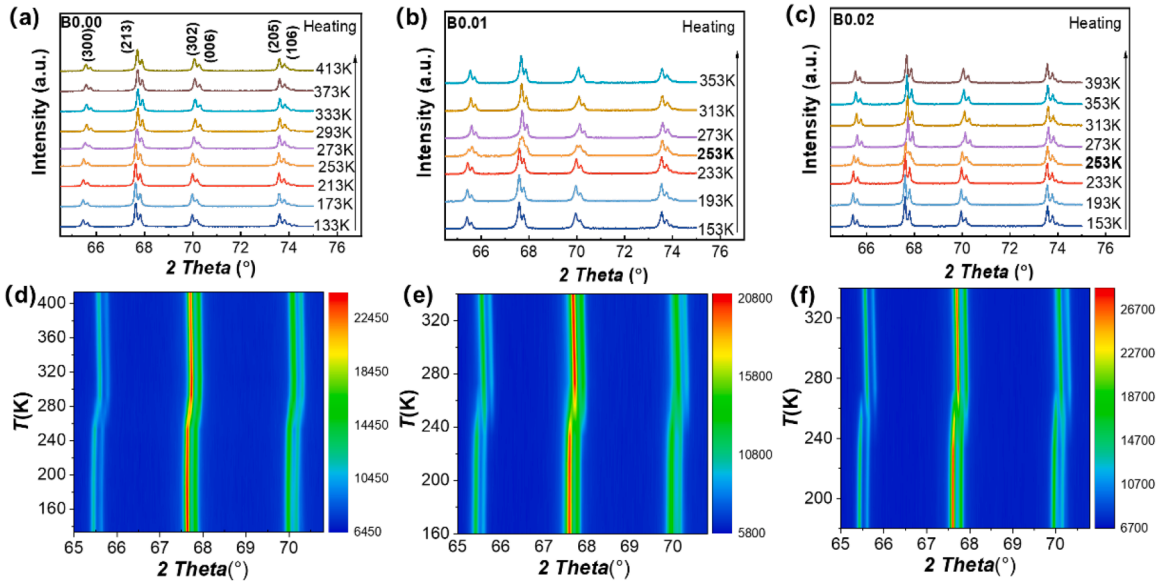

Fig. 8. (a-c) XRD patterns as a function of the scattering angle, recorded upon heating for the B0.00, B0.01 and B0.02 alloys. (d-e) Intensity contour map showing the evolution of several Bragg peaks across the magnetoelastic transition in the above alloys.

The extremely low α_l for B0.01 is much smaller than the value for conventional NTE materials such as the Invar alloy $Fe_{65}Ni_{35}$ (α_l = 1.5 ppm/K, 193–373 K) [1] and $Y_2Mo_3O_{12}$ (α_l = 9.02 ppm/K, 20–450 K) [48], as listed in Table 1. It is also lower than those of magnetic ZTE materials, including $Mn_{0.975}Ni_{0.025}CoSi$, (α_l = 0.13 ppm/K, 10–170), $LaFe_{11}Si_2$ hydride (α_l = 0.5 ppm/K, 20–275) and $Mn_3Zn_{0.93}N$ (α_l = 0.6 ppm/K, 4–185), where the ZTE occurs prior to the magnetoelastic transition. As summarized in Table 1, compared with the conventional NTE materials, the magnetic NTE materials generally exhibit a narrower NTE/ZTE temperature range, but lower CTE values. The thermal hysteresis extracted from the *M-T* curves and DSC measurements is 1–2 K and 3–6 K, respectively, for all the $Fe_{1.98}Hf_{0.85}Ta_{0.15}B_x$ (x = 0.00–0.04) alloys. This small hysteresis originates from the magnetoelastic transition in $Fe_2(Hf,Ta)$-based alloys, in contrast to the much larger thermal hysteresis (~20 K) typically observed in hexagonal MnCoGe-based alloys undergoing a magnetostructural transition [49].

In most magnetocaloric materials, the ZTE originates from the suppression or broadening of a magnetic transition through chemical modifications, as observed in systems like $(Zr_{1-x}Nb_x)Fe_2$ [17], $R_2(Fe,Co)_{17}$ [24], $Sc_{0.55}Ti_{0.45}Fe_2$ [16], $TbCo_{2-x}Fe_x$ [56], $ErCo_{2.8}Fe_{0.2}$ [8], antiperovskite manganese nitride [22] and $LaFe_{13-x}Al_x$ [59]. However, in the B0.01 and B0.02 alloys, the ZTE occurs below the magnetoelastic transition, similar to that reported in $La(Fe,Si)_{13}$ hydrides [12], $Mn_{1-x}Ni_xCoSi$ [58]. and $Mn_3Cu_{0.5}Ge_{0.5}N$ alloys [22], suggesting a different origin. As shown in Fig. 10, the B0.01 alloy exhibits a much sharper dM/dT than the B0.00 alloy, consistent with a FOMT in B0.01

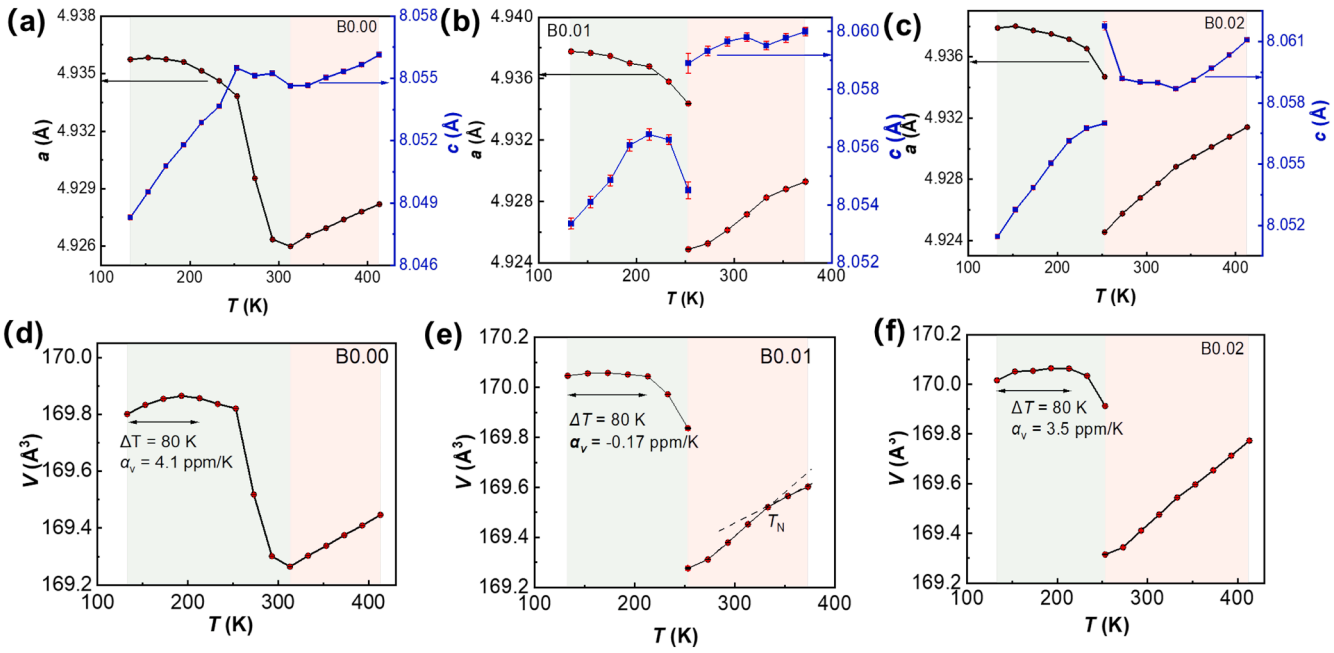

Fig. 9. Temperature dependence of (a, b, c) lattice parameters *a* and *c* and (d, e, f) unit-cell volume *V* for the B0.00, B0.01 and B0.02 alloys.

Table 1
Linear thermal expansion data (α_l), temperature range (ΔT) and crystal structure of a series of conventional and magnetic NTE materials. * For materials with anisotropic thermal expansion, the value of α_l is estimated as one-third of the volumetric CTE (α_V).

Compounds	Crystal structure	ΔT (K)	α_l($\times 10^{-6}$ K^{-1})	Ref.
ScF_3	Cubic	10–1100	−4.97	[50]
$ZrMo_2O_8$	Cubic	250–502	−5.0	[51]
$HfMo_2O_8$	Cubic	77–573	−4.0	[52]
ZrW_2O_8	Cubic	2–1443	−7.2	[53,54]
Invar 35	Cubic	193–373	1.5	[1]
ReO_3	Cubic	2–400	0.7	[55]
$Y_2Mo_3O_{12}$	Orth.	20–450	−9.02	[48]
$Fe_{1.98}Hf_{0.85}Ta_{0.15}$	Hex.	133–213	1.37*	This work
$Fe_{1.98}Hf_{0.85}Ta_{0.15}B_{0.01}$			−0.06*	This work
$Fe_{1.98}Hf_{0.85}Ta_{0.15}B_{0.02}$			1.17*	This work
$LaFe_{11}Si_2$ hydride	Cubic	20–275	0.5	[12]
$TbCo_{1.9}Fe_{0.1}$	Cubic	123–307	0.48	[56]
$Mn_3Zn_{0.93}N$	Cubic	4–185	0.6	[57]
$Mn_{0.975}Ni_{0.025}CoSi$	Hex.	10–170	0.13	[58]

and a SOMT in B0.00. The NTE emerges in the temperature region corresponding to the lowest $|dM/dT|$ values, highlighting the strong magnetoelastic coupling in this system. The magnetic-lattice coupling can be quantitatively described by the relation: $\omega_s(T) = kCM(T)^2$, where k and C are the compressibility and the magneotoelastic coupling parameter, and kC represents the magnetoelastic coupling strength [47,60]. Here, M denotes the local magnetic moment measured under a 1 T magnetic field, and ω_s is the magnetic contribution to thermal expansion. The latter is determined as: $\omega_s = \omega_{exp} - \omega_{nm}$, where ω_{exp} is the experimental thermal expansion, and ω_{nm} is the phonon anharmonic vibration contribution to thermal expansion, estimated from the linear fitting of the high-temperature thermal expansion [61]. Similar trends for the extracted ω_s and M^2, as shown in Fig. 10(c-d) confirm the critical role of the magnetoelastic coupling in stabilizing the ZTE and enabling a tunable NTE [25]. Notably, the coupling constant kC increases from 1.30 $\times 10^{-10}$ cm^2/A^2 for B0.00 to 1.69 $\times 10^{-10}$ cm^2/A^2 for B0.01, indicating stronger coupling between magnetization and lattice after B doping [8,47]. These kC values are of the same order of magnitude as those for $Fe_2Hf_{0.85}Ti_{0.15}$ (1.48 $\times 10^{-10}$ cm^2/A^2) [62], $Fe_2Hf_{0.83}Ta_{0.17}$ with (1.32 $\times 10^{-10}$ cm^2/A^2) [28] and $La(Fe_{0.86}Al_{0.24})_{13}$ with (1.79 $\times 10^{-10}$ cm^2/A^2) [63], which are magnetic NTE materials with a strong magnetoelastic coupling.

In magnetically driven NTE systems, the CTE is governed by magnetic interactions. For Fe_2(Hf,Ta) alloys, the sharp FM-AFM transition originates from the frustration of Fe moments at the 2*a* sites, which are located between the AFM-coupled Fe(6*h*) layers [25,39,64]. The magnetoelastic transition is highly sensitive to the lattice strain, which is inevitably introduced by elemental doping, which is inevitably introduced by elemental doping [65,66]. Unlike Co [67] or Mn [68] doping, which tends to broaden the transition, trace small atoms substitutions such as C [7] or B atoms sharpen the FOMT, leading to a ZTE prior to the AFM-FM transition. In particular, Mn tends to occupy the 6*h* site [68], which responses to normal thermal expansion before the AFM-FM transition, in contrast to the effect of B atoms. In Fe_2(Hf,Ta) Laves phase alloys with a highly symmetric Kagome structure, substitutional B atoms occupy the Fe 2*a* site by DFT calculations, leading to an atomic size mismatch and local electron concentration variations, that is a 5.6 % decrease in Fe(2*a*)-Hf orbital localization and, simultaneously, a 5.0 % increase in Fe(6*h*)-Hf localization. This redistribution modifies the frustration effect of 2*a* sites and enhances the magnetoelastic coupling, thereby giving rise to ZTE prior to the AFM-FM transition for B-doped Fe_2(Hf,Ta) alloys.

4. Conclusions

In this study, the effect of B doping on the magnetoelastic transition, thermal expansion and magnetocaloric effects in Fe_2(Hf,Ta)B$_x$ Laves phase alloys has been investigated systematically. Increasing the B content leads to a clear contraction of the lattice volume, accompanied by a shift in the magnetic transition temperature. The B0.00 alloy displays a SOMT with a $|\Delta S_M|$ value of 3.91 J/kgK in a magnetic field change of 5 T B-doped alloys with $x = 0.01$ and 0.02 undergo a FOMT, along with enhanced $|\Delta S_M|$ values of 4.29 and 3.52 J/kgK, respectively, for the same magnetic field change. Boron doping not only enhances the hardness of the Fe_2(Hf,Ta)B$_x$ alloys, but also increases the sensitivity of

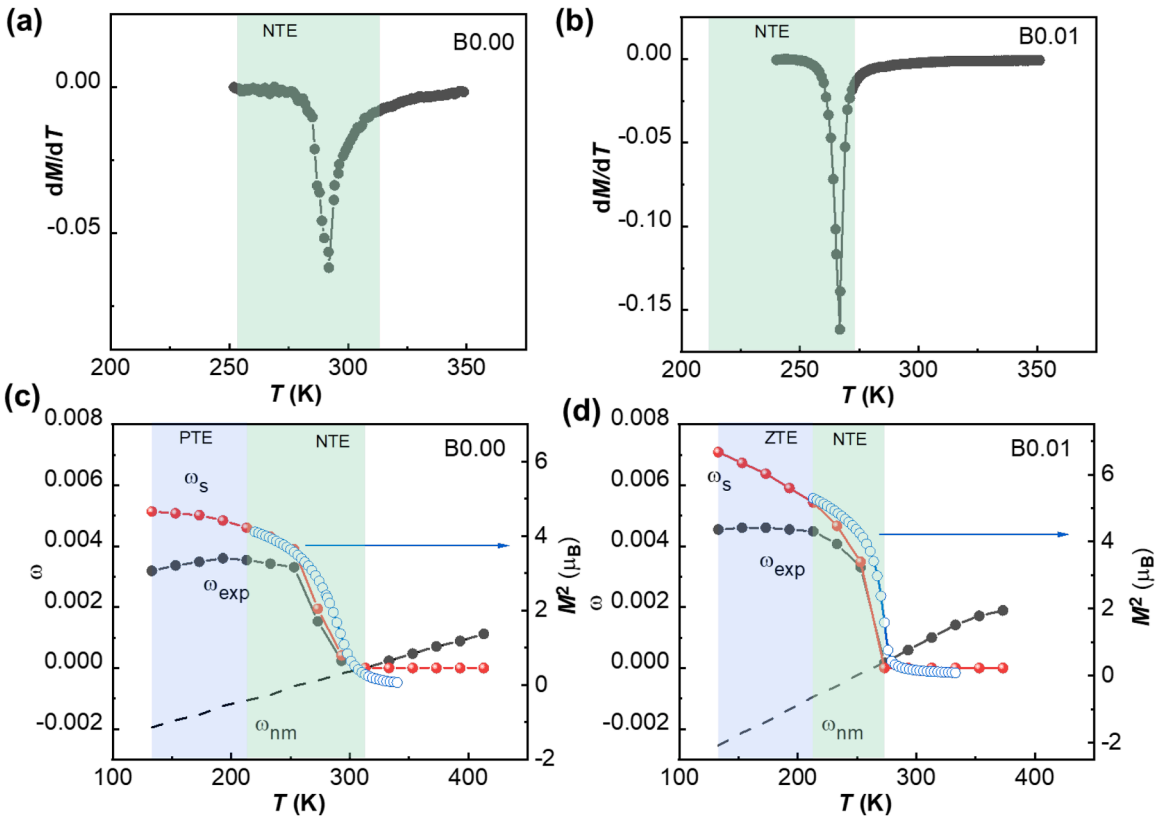

Fig. 10. (a) First derivative of magnetization (dM/dT) under a 1 T magnetic field for B0.00 and (b) B0.01. Temperature dependence of the spontaneous magnetostriction ω_s, experimental thermal expansion ω_{exp}, nonmagnetic contribution to thermal expansion ω_{nm}, and squared magnetization M^2 for (c) B0.00 and (d) B0.01. The temperature ranges corresponding to ZTE, NTE, and PTE are highlighted in different colors.

the magnetoelastic transition temperature to the applied magnetic field. Furthermore, the B0.01 alloy exhibits a near-zero CTE of –0.17 ppm/K over a wide temperature range of 133–213 K, accompanied a strong magnetoelastic coupling. First-principles calculations reveal that the B atoms preferentially occupy the Fe 2*a* crystallographic site, modifying the electronic structure through an altered Fe-Hf hybridization. This electronic restructuring drives the stronger magnetoelastic coupling and gives rise to ZTE prior to the AFM-FM transition in B-doped Fe_2(Hf,Ta) alloys.

CRediT authorship contribution statement

Qi Shen: Writing – original draft, Supervision, Project administration, Funding acquisition, Formal analysis. **Zeyu Zhang:** Methodology, Investigation, Formal analysis, Data curation. **Weixiang Hao:** Software, Data curation. **Niels van Dijk:** Writing – review & editing. **Ekkes Brück:** Writing – review & editing. **Lingwei Li:** Writing – review & editing, Project administration.

Declaration of competing interest

The authors declare that they have no known competing financial interests or personal relationships that could have appeared to influence the work reported in this paper.

Acknowledgements

This work was financially supported by National Natural Science Foundation of China (Grant No 52401230, 52472274) and Zhejiang Provincial Natural Science Foundation of China (Grant No ZCLMS25E0101). The authors acknowledge the Supercomputing Center of Hangzhou Dianzi University for providing computing resources.

Supplementary materials

Supplementary material associated with this article can be found, in the online version, at doi:10.1016/j.actamat.2025.121687.

References

[1] C.E. Guillaume, Recherches sur les aciers au nickel. Dilatations aux temperatures elevees; resistance electrique, CR Acad. Sci. 125 (1) (1897) 235–238.
[2] O. Tegus, E. Bruck, K.H.J. Buschow, F.R.d. Boer, Transition-metal-based magnetic refrigerants for room-temperature applications, Nature 415 (2002) 150–151.
[3] Y. Zhang, W. Hao, H.-F. Li, L.W. Li, Apatite-type gadolinium-based dense $MGd_4Si_3O_{13}$ (M = Mg, Ca, and Sr) ceramics: an emerging class of sub-liquid helium temperature magnetic refrigerant, Acta Mater. 292 (2025) 121033.
[4] J. Liu, T. Gottschall, K.P. Skokov, J.D. Moore, O. Gutfleisch, Giant magnetocaloric effect driven by structural transitions, Nat. Mater. 11 (7) (2012) 620–626.
[5] T. Gottschall, K.P. Skokov, M. Fries, A. Taubel, I. Radulov, F. Scheibel, D. Benke, S. Riegg, O. Gutfleisch, Making a cool choice: the Materials Library of Magnetic refrigeration, Adv. Energy Mater. 9 (34) (2019) 1901322.
[6] F. Chen, J. Xu, X. Zhao, Y. Na, Y. Zhang, Structural and magnetic characterization of weberite-type RE_3NbO_7 (*RE* = Gd, Dy, Ho and Er) ceramics featuring notable cryogenic magnetocaloric responses, Sci. China Mater. 68 (2025) 2828.
[7] J. Xu, Z. Wang, H. Huang, Z. Li, X. Chi, D. Wang, J. Zhang, X. Zheng, J. Shen, W. Zhou, Y. Gao, J. Cai, T. Zhao, S. Wang, Y. Zhang, B. Shen, Significant zero thermal expansion via enhanced magnetoelastic coupling in kagome magnets, Adv. Mater. 35 (8) (2023) 2208635.
[8] J. Xu, G. Wang, S. Xing, L. Xi, J. Sheng, S. Li, X. Kan, M. Zheng, Y. Gao, D. Wang, X. Zheng, J. Zhang, J. Xu, W. Yin, S. Zhou, B. Shen, S. Wang, Zero thermal expansion via the unconventional sublattice-magnetovolume effect in rare-earth ferrimagnets, Adv. Func. Mater. 35 (2024) 2416314.
[9] H.-B. Zhou, Z.-B. Yu, F.-x. Hu, J.-T. Wang, F.-R. Shen, J.-Z. Hao, L.-H. He, Q.-Z. Huang, Y.-H. Gao, B.-J. Wang, Z. Yin, Z.-Y. Tian, J. Wang, Y.-Z. Chen, J.-R. Sun, T.-Y. Zhao, B.-G. Shen, Emergence of Invar effect with excellent mechanical property by electronic structure modulation in $LaFe_{11.6-x}Co_xSi_{1.4}$ magnetocaloric materials, Acta Mater. 260 (2023) 119312.
[10] W. Wang, R. Huang, W. Li, J. Tan, Y. Zhao, S. Li, C. Huang, L. Li, Zero thermal expansion in $NaZn_{13}$-type La(Fe,Si)$_{13}$ compounds, Phys. Chem. Chem. Phys. 17 (4) (2015) 2352–2356.

[11] R. Huang, Y. Liu, W. Fan, J. Tan, F. Xiao, L. Qian, L. Li, Giant negative thermal expansion in $NaZn_{13}$-type La(Fe, Si, Co)$_{13}$ compounds, J. Am. Chem. Soc. 135 (31) (2013) 11469–11472.

[12] S. Li, R. Huang, Y. Zhao, W. Wang, Y. Han, L. Li, Zero thermal expansion achieved by an electrolytic hydriding method in La(Fe,Si)$_{13}$ compounds, Adv. Func. Mater. 27 (5) (2016) 1604195.

[13] Y. Liu, J. Li, Y. Qian, S. Qie, S. Mi, Z. Xu, H. Xie, X. Song, T. Ma, Isotropic negative thermal expansion in the multiple-phase La-Fe-Co-Si alloys with enhanced strength and ductility, Acta Mater. 275 (2024) 120058.

[14] B. Li, X.H. Luo, H. Wang, W.J. Ren, S. Yano, C.W. Wang, J.S. Gardner, K.D. Liss, P. Miao, S.H. Lee, T. Kamiyama, R.Q. Wu, Y. Kawakita, Z.D. Zhang, Colossal negative thermal expansion induced by magnetic phase competition on frustrated lattices in laves phase compound (Hf,Ta)Fe_2, Phys. Rev. B 93 (22) (2016) 224405.

[15] Y. Qiao, Y. Song, K. Lin, X. Liu, A. Franz, Y. Ren, J. Deng, R. Huang, L. Li, J. Chen, X. Xing, Negative thermal expansion in (Hf,Ti)Fe_2 induced by the ferromagnetic and antiferromagnetic phase coexistence, Inorg. Chem. 58 (9) (2019) 5380–5383.

[16] Y. Song, Q. Sun, M. Xu, J. Zhang, Y. Hao, Y. Qiao, S. Zhang, Q. Huang, X. Xing, J. Chen, Negative thermal expansion in (*Sc*,Ti)Fe_2 induced by an unconventional magnetovolume effect, Mater. Horiz. 7 (1) (2020) 275–281.

[17] Y. Song, Q. Sun, T. Yokoyama, H. Zhu, Q. Li, R. Huang, Y. Ren, Q. Huang, X. Xing, J. Chen, Transforming thermal expansion from positive to negative: the case of cubic magnetic compounds of (Zr,Nb)Fe_2, J. Phys. Chem. Lett. 11 (5) (2020) 1954–1961.

[18] W. Li, K. Lin, Y. Yan, C. Yu, Y. Cao, X. Chen, C.W. Wang, K. Kato, Y. Chen, K. An, Q. Zhang, L. Gu, Q. Li, J. Deng, X. Xing, A seawater-corrosion-resistant and isotropic zero thermal expansion (Zr,Ta)(Fe,Co)$_2$ alloy, Adv. Mater. 34 (34) (2022) 2109592.

[19] M. Xu, Q. Li, Y. Song, Y. Xu, A. Sanson, N. Shi, N. Wang, Q. Sun, C. Wang, X. Chen, Y. Qiao, F. Long, H. Liu, Q. Zhang, A. Venier, Y. Ren, F. d'Acapito, L. Olivi, D.O. De Souza, X. Xing, J. Chen, Giant uniaxial negative thermal expansion in $FeZr_2$ alloy over a wide temperature range, Nat. Commun. 14 (1) (2023) 4439.

[20] Q. Shen, Z. Zhang, C. de Vries, A.I. Dugulan, N. van Dijk, E. Brück, L. Li, Zero thermal expansion effect and enhanced magnetocaloric effect induced by Fe vacancies in $Fe_2Hf_{0.80}Nb_{0.20}$ laves phase alloys, Chem. Mater. 36 (12) (2024) 6299–6305.

[21] R.Y. Yanming Sun, Sergii Khmelevskyi, Kenichi Kato, Yili Cao, Shixin Hu, Maxim Avdeev, Chin-Wei Wang, Chengyi Yu, Qiang Li, Kun Lin, Xiaojun Kuang, Xianran Xing, Local chemical heterogeneity enabled superior zero thermal expansion in nonstoichiometric pyrochlore magnets, Nat. Sci. Rev. 12 (2025) nwae462.

[22] X. Song, Z. Sun, Q. Huang, M. Rettenmayr, X. Liu, M. Seyring, G. Li, G. Rao, F. Yin, Adjustable zero thermal expansion in antiperovskite manganese nitride, Adv. Mater. 23 (40) (2011) 4690–4694.

[23] S. Deng, Y. Sun, H. Wu, Z. Shi, L. Wang, J. Yan, K. Shi, P. Hu, X. Diao, Q. Huang, C. Sürgers, C. Wang, Phase separation and zero thermal expansion in antiperovskite $Mn_3Zn_{0.77}Mn_{0.19}N_{0.94}$: an in situ neutron diffraction investigation, Scr. Mater. 146 (2018) 18–21.

[24] Y. Cao, K. Lin, S. Khmelevskyi, M. Avdeev, K.M. Taddei, Q. Zhang, Q. Huang, Q. Li, K. Kato, C.C. Tang, A. Gibbs, C.-W. Wang, J. Deng, J. Chen, H. Zhang, X. Xing, Ultrawide temperature range super-invar behavior of R_2(Fe,Co)$_{17}$ materials (R= Rare Earth), Phys. Rev. Lett. 127 (5) (2021) 055501.

[25] L.F. Li, P. Tong, Y.M. Zou, W. Tong, W.B. Jiang, Y. Jiang, X.K. Zhang, J.C. Lin, M. Wang, C. Yang, X.B. Zhu, W.H. Song, Y.P. Sun, Good comprehensive performance of laves phase $Hf_{1-x}Ta_xFe_2$ as negative thermal expansion materials, Acta Mater. 161 (2018) 258–265.

[26] H. Wang, Y.H. Wang, Y.Y. Gong, G.Z. Xu, E. Liu, X.F. Miao, Y.J. Zhang, Y.Y. Shao, J. Liu, N. Ui Hassan, I.A. Shah, F. Xu, Designing (Hf,Ta)Fe_2-based zero thermal expansion composites consisting of multiple laves phases, Rare Metals 43 (2024) 6596–6605.

[27] J.F. Herbst, C.D. Fuerst, R.D. McMichael, Structural, magnetic, and magnetocaloric properties of $(Hf_{0.83}Ta_{0.17})Fe_{2+x}$ materials, J. Appl. Phys. 79 (8) (1996) 5998.

[28] Q. Shen, F. Zhang, I. Dugulan, N. van Dijk, E. Brück, Magnetoelastic transition and negative thermal expansion of $Fe_2Hf_{0.83}Ta_{0.17}$ ribbons, Scr. Mater. 232 (2023) 115482.

[29] B.H. Toby, R factors in Rietveld analysis: how good is good enough? Powder Diffr. 21 (1) (2006) 67–70.

[30] G. Kresse, J. Hafner, Ab initio molecular dynamics for liquid metals, Phys. Rev. B Condens. Matter. 47 (1) (1993) 558–561.

[31] J.F.G. Kresse, Efficiency of ab-initio total energy calculations for metals and semiconductors using a plane-wave basis set, Comput. Mater. Sci. 6 (1996) 15–50.

[32] P.E. Blochl, Projector augmented-wave method, Phys. Rev. B Condens. Matter. 50 (24) (1994) 17953–17979.

[33] G.K.D. Joubert, From ultrasoft pseudopotentials to the projector augmented-wave method, Phys. Rev. B 59 (1999) 1758–1775.

[34] K.B. John, P. Perdew, Matthias Ernzerhof, Generalized gradient approximation made simple, Phys. Rev. Lett. 77 (18) (1996) 3865–3868.

[35] A.S.B. Silvi, Classification of chemical-bonds based on topological analysis of electron localization functions, Nature 371 (1994) 683–686.

[36] J.Y. Law, V. Franco, L.M. Moreno-Ramirez, A. Conde, D.Y. Karpenkov, I. Radulov, K.P. Skokov, O. Gutfleisch, A quantitative criterion for determining the order of magnetic phase transitions using the magnetocaloric effect, Nat. Commun. 9 (1) (2018) 2680.

[37] Y. Zhang, W. Hao, C. Hu, X. Wang, X. Zhang, L. Li, Rare-earth-free $Mn_{30}Fe_{20-x}Cu_xAl_{50}$ magnetocaloric materials with stable cubic CsCl-type structure for room-temperature refrigeration, Adv. Func. Mater. 33 (52) (2023) 2310047.

[38] Z. Song, Z. Li, B. Yang, H. Yan, C. Esling, X. Zhao, L. Zuo, Large low-field reversible magnetocaloric effect in itinerant-electron $Hf_{1-x}Ta_xFe_2$ alloys, Materials (Basel) 14 (18) (2021) 1–11.

[39] L.V.B. Diop, O. Isnard, M. Amara, F. Gay, J.P. Itié, Giant negative thermal expansion across the first-order magnetoelastic transition in $Hf_{0.86}Ta_{0.14}Fe_2$, J. Alloys Compd. 845 (2020) 156310.

[40] L. Caron, X.F. Miao, J.C.P. Klaasse, S. Gama, E. Brück, Tuning the giant inverse magnetocaloric effect in $Mn_{2-x}Cr_xSb$ compounds, Appl. Phys. Lett. 103 (11) (2013) 112404.

[41] Q. Shen, I. Batashev, H. Ojiyed, F. Zhang, N. van Dijk, E. Brück, Nonlinear influence of excess Mn on the magnetoelastic transition in (Mn,Cr)$_2$Sb, J. Alloys Compd. 903 (2022) 164011.

[42] J. Lyubina, Magnetocaloric materials for energy efficient cooling, J. Phys. D: Appl. Phys. 50 (5) (2017) 053002.

[43] F. Zhang, I. Batashev, Q. Shen, Z. Wu, R.I. Smith, G.A. de Wijs, N. van Dijk, E. Brück, Impact of F and S doping on (Mn,Fe)$_2$(P,Si) giant magnetocaloric materials, Acta Mater. 234 (2022) 118057.

[44] J. Liu, Y. You, I. Batashev, Y. Gong, X. You, B. Huang, F. Zhang, X. Miao, F. Xu, N. van Dijk, E. Brück, Design of reversible low-field magnetocaloric effect at room temperature in hexagonal MnMX ferromagnets, Phys. Rev. Appl. 13 (5) (2020) 054003.

[45] F. Zhang, I. Batashev, N. van Dijk, E. Bruck, Reduced hysteresis and enhanced giant magnetocaloric effect in B-doped all-D-metal Ni-Co-Mn-Ti-based heusler materials, Phys. Rev. Appl. 17 (5) (2022) 054032.

[46] Q. Shen, N. van Dijk, E. Brück, L. Li, Exploring zero thermal expansion in magnetocaloric materials, Adv. Eng. Mater. (2025) 2500833.

[47] J. Chen, L. Hu, J. Deng, X. Xing, Negative thermal expansion in functional materials: controllable thermal expansion by chemical modifications, Chem. Soc. Rev. 44 (11) (2015) 3522–3567.

[48] B.A. Marinkovic, M. Ari, R.R. de Avillez, F. Rizzo, F.F. Ferreira, K.J. Miller, M. B. Johnson, M.A. White, Correlation between AO_6 polyhedral distortion and negative thermal expansion in orthorhombic $Y_2Mo_3O_{12}$ and related materials, Chem. Mater. 21 (13) (2009) 2886–2894.

[49] X. Hao, Y. Zhao, X. Huang, K. Liu, B. Zhao, C. Zhang, J. Ma, F. Qian, X. Miao, Y. Kuang, H. Yan, Z. Li, L. Zuo, X. Tong, B. Yang, Q. Ren, In-situ study of the temperature effects on the magneto-structural transition in the MnCoGe-based magnetocaloric compounds, Acta Mater 296 (2025) 121241.

[50] Benjamin K. Greve, Kenneth L. Martin, Peter L. Lee, Peter J. Chupas, Karena W. Chapman, Angus P. Wilkinson, Pronounced negative thermal expansion from a simple structure: cubic ScF_3, J. Am. Chem. Soc. 132 (2010) 15496–15498.

[51] S. Allen, J.S.O. Evans, Negative thermal expansion and oxygen disorder in cubic $ZrMo_2O_8$, Phys. Rev. B 68 (13) (2003) 134101.

[52] Catherine A. Kennedy, Mary Anne White, Angus P. Wilkinson, Tamas Varga, Low thermal conductivity of the negative thermal expansion material, $HfMo_2O_8$, Appl. Phys. Lett. 90 (2007) 151906.

[53] T.A. Mary, J.S.O. Evans, T. Vogt, A.W. Sleight, Negative thermal expansion from 0.3 to 1050 kelvin in ZrW_2O_8, Science 272 (1996) 92–94.

[54] J.S.O. Evans, Negative thermal expansion materials, J. Chem. Soc., Dalton Trans. (19) (1999) 3317–3326.

[55] Tapan Chatterji, Thomas C. Hansen, Michela Brunelli, P.F. Henry, Negative thermal expansion of ReO3 in the extended temperature range, 94 (2009) 241902.

[56] Y. Song, J. Chen, X. Liu, C. Wang, J. Zhang, H. Liu, H. Zhu, L. Hu, K. Lin, S. Zhang, X. Xing, Zero thermal expansion in magnetic and metallic Tb(Co,Fe)$_2$ intermetallic compounds, J. Am. Chem. Soc. 140 (2) (2018) 602–605.

[57] C. Wang, L. Chu, Q. Yao, Y. Sun, M. Wu, L. Ding, J. Yan, Y. Na, W. Tang, G. Li, Q. Huang, J.W. Lynn, Tuning the range, magnitude, and sign of the thermal expansion in intermetallic $Mn_3(Zn,M)_xN$ (M = Ag, Ge), Phys. Rev. B 85 (22) (2012) 220103.

[58] J. Liu, B. Ding, Y. Yao, X. Xi, Z. Cheng, J. Wang, C.-w. Wang, G. Wu, W. Wang, Coherent spin rotation-induced zero thermal expansion in MnCoSi-based spiral magnets, NPG Asia Mater 13 (1) (2021) 70.

[59] W. Li, R. Huang, W. Wang, Y. Zhao, S. Li, C. Huang, L. Li, Abnormal thermal expansion properties of cubic $NaZn_{13}$-type La(Fe,Al)$_{13}$ compounds, Phys. Chem. Chem. Phys. 17 (8) (2015) 5556–5560.

[60] Y. Song, N. Shi, S. Deng, X. Xing, J. Chen, Negative thermal expansion in magnetic materials, Prog. Mater. Sci. 121 (2021) 100835.

[61] Y. Takahashi, H. Nakano, Magnetovolume effect of itinerant electron ferromagnets, J. Phys. Condens. 18 (2) (2006) 521–556.

[62] Q. Shen, I. Batashev, F. Zhang, H. Ojiyed, I. Dugulan, N. van Dijk, E. Brück, Exploring the negative thermal expansion and magnetocaloric effect in Fe_2(Hf,Ti) laves phase materials, Acta Mater. 257 (2023) 119149.

[63] T.T. Palstra, G.J. Nieuwenhuys, J.A. Mydosh, K.H. Buschow, Mictomagnetic, ferromagnetic, and antiferromagnetic transitions in La(Fe$_x$Al$_{1-x}$)$_{13}$ intermetallic compounds, Phys. Rev. B 31 (7) (1985) 4622–4632.

[64] H.R. Rechenberg, L. Morellon, P.A. Algarabel, M.R. Ibarra, Magnetic moment at highly frustrated sites of antiferromagnetic laves phase structures, Phys. Rev. B 71 (10) (2005) 104412.

[65] S. Iikubo, K. Kodama, K. Takenaka, H. Takagi, M. Takigawa, S. Shamoto, Local lattice distortion in the giant negative thermal expansion material $Mn_3Cu_{1-x}Ge_xN$, Phys. Rev. Lett. 101 (20) (2008) 205901.

[66] J. Matsuno, K. Takenaka, H. Takagi, D. Matsumura, Y. Nishihata, J. Mizuki, Local structure anomaly around Ge dopants in $Mn_3Cu_{0.7}Ge_{0.3}N$ with negative thermal expansion, Appl. Phys. Lett. 94 (2009) 181904.
[67] Y. Huang, Z. Han, Z. Jiang, S. Li, Y. Hsia, Microscopic magnetic properties of itinerant-electron system $Hf_{0.8}Ta_{0.2}(Fe_{1-x}Co_x)_2$ (x=0–0.09): a Mössbauer study, Physica B: Condens. Matter 388 (1–2) (2007) 354–358.
[68] Q. Shen, F. van Rooij, Z. Zhang, W. Hao, A.I. Dugulan, N. van Dijk, E. Brück, L. Li, Tunable magnetoelastic transition and enhanced magnetocaloric response in $Hf_{0.82}Ta_{0.18}Fe_2$ laves phase alloys by Fe(6*h*)-site manipulation, J. Mater. Sci. Technol. 254 (2025) 196–205.